Iron nitrides substituted with transition metals: DFT study of promising systems for anomalous Nernst effect

Kyo-Hoon Ahn , Jakub Vít , Mariia Pashchenko , and Karel Knížek [*]

Institute of Physics of the CAS, Cukrovarnická 10, 162 00 Praha 6, Czech Republic

The anomalous Nernst effect is studied by *ab initio* calculations in substituted iron nitrides with antiperovskite structure Fe_3M^1N and $Fe_2M^1M^2N$ ($M^1 = 4d$ or $5d$, and $M^2 = 3d$ transition metals), considering the intrinsic Berry curvature-related mechanism depending only on the band structure. The highest absolute anomalous Nernst conductivity (ANC) 8 $A K^{-1} m^{-1}$ with a negative sign is calculated for ruthenium substituted ferromagnetic phase Fe_3RuN. A similar maximum ANC is determined for ferrimagnetic phase Fe_2RuCrN, yet the advantage of this doubly substituted phase is that the high ANC values persist over a wider temperature range. Comparable ANCs have so far only been determined for compounds with critical temperatures of magnetic ordering below room temperature, while substituted iron nitrides exhibit T_C well above room temperature. Therefore, we propose Fe_2RuCrN, composed from nontoxic, and except for Ru, also fairly abundant elements, as a starting stoichiometry for further experimental study of candidates for devices possessing a high ANC and suitable for room- and high-temperature applications.

I. INTRODUCTION

Iron nitrides Fe_xN ($x \geqslant 3$) [1] are commercially important compounds because of their versatile magnetic, electrical, and mechanical properties [2–7]. Since they only consist of iron and nitrogen, which are both cheap, abundant, and nontoxic, they provide environmentally friendly and recyclable functional materials. The interest in iron nitrides originated from their use for industrial surface hardening of steel [8,9]. Later, their application potential expanded due to their excellent magnetic properties, which offered applications as high-density magnetic recording heads and magnetic recording media, and in biomedical fields due to low cytotoxicity [10–14]. Recently, significant transverse thermomagnetic properties were discovered in epitaxial Fe_4N films on various substrates [15,16], where the coefficient of the anomalous Nernst effect (ANE) up to 2.8 μV/K was obtained in the Fe_4N film on the $SrTiO_3$(001) substrate. This discovery further expanded the possible application of iron nitrides for thermoelectric energy harvesting [17–22].

The structure of Fe_4N [Fig. 1(b)] is derived from the fcc structure of γ-Fe [Fig. 1(a)] by inserting a nitrogen atom into the center of the cube. It is described by a cubic $Pm\bar{3}m$ space group, where N occupies the body center with Wyckoff position 1b, and three Fe ions occupy the face centers in position 3c, while another Fe atom occupies the corners in position 1a [23,24]. An alternative description of the structure is as an antiperovskite ABX_3, if the formula is written as $FeNFe_3$. It means that nitrogen is located in the position of a small cation B in the center of the BX_6 (NFe_6) octahedron, and iron is in

two crystallographic positions, i.e., in the position of a big cation A and as ligands X of the BX_6 (NFe_6) octahedron.

The transverse transport refers to the arrangement when two external fields, aligned along two perpendicular axes of the sample, induce charge or entropy density flows along the third remaining axis of the sample. For the Nernst effect, one of these stimulating fields is the thermal gradient ∇T and the other one is the orthogonally oriented magnetic field $\boldsymbol{B}$ or the spontaneous magnetization $\boldsymbol{M}$. The transverse transport is revealed generally as the Nernst voltage V_N in the direction of the third axis perpendicular to both ∇T and $\boldsymbol{B}$ ($\boldsymbol{M}$).

The total signal of the Nernst effect (S_{xy}) is composed of the ordinary Nernst effect (S_{xy}^O), which is linearly proportional to the applied magnetic field, and the ANE (S_{xy}^A), which follows the field dependence of magnetization, according to the relation

$$S_{xy} = S_{xy}^O B_z + S_{xy}^A(M_z). \tag{1}$$

One of the possible mechanisms for the appearance of the ANE is connected with the Berry curvature. The effect of the Berry curvature is that it acts as an intense magnetic field (local in the reciprocal space), so it exerts a strong force on charge carriers. The emergence of the Berry curvature is closely related to the presence of Weyl points, which act as magnetic monopoles in the reciprocal space under the spin-orbit coupling (SOC), and play a role of sources or sinks of the Berry curvature of Bloch wave functions. The effect of the SOC on the band structure increases the probability of the occurrence of suitable band splitting with potentially diverging the Berry curvature. Therefore the presence of elements exhibiting a strong SOC may favor an increase of the ANE [25–27]. In general, the strength of the SOC increases with increasing atomic number, so we will first look for
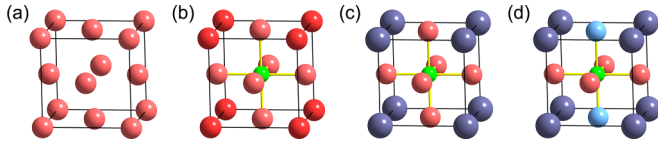
*Corresponding author: knizek@fzu.cz

FIG. 1. Structures of (a) γ-Fe, (b) Fe$_4$N, (c) Fe$_3$RuN, and (d) Fe$_2$RuCrN. Bullets: green, N; pink, Fe in $3c$ site (1/2,1/2,0), red, Fe in $1a$ site (0,0,0); blue, Ru in $1a$ site; and light blue, Cr in 1/3 of $3c$ site.

possible candidates for doping among heavy transition metals (TMs) from the $4d$ (Ru, Rh) and $5d$ (Os, Ir) row in the periodic table.

Such compounds were only rarely produced [28–30]. Fe$_3$RhN was successfully synthesized by one group only [29,30], while Ru, Os, and Ir-substituted Fe$_4$N were prepared only up to 0.2 content of the substituted ion per formula unit [28] by the coprecipitation method. In all cases, larger $4d$ or $5d$ ions replace Fe at $1a$ Wyckoff position, which is ascribed to its larger space compared to the $3c$ position [28–30]. Due to difficulty of the synthesis, most investigations of these compounds were theoretical [31–42].

A necessary condition for meaningful theoretical investigation is the mechanical stability of a compound, which describes stability with respect to infinitesimally small variations of atomic positions. Several works proved that all Fe$_3$(Ru,Rh,Os,Ir)N compounds are mechanically stable [31,34,38,40]. Nevertheless, the mechanical stability means only a local energy minimum, while the global minimum may be different, which may prevent synthesizing of the compounds or they may degrade in time. In order to predict conditions for the synthesis, the formation enthalpy was calculated for the Fe$_3$(Ru,Rh,Os,Ir)N compounds, showing that only Fe$_3$RhN is stable [33], while Fe$_3$(Ru,Os,Ir)N do not represent the global energy minimum at ambient conditions [33,35], which makes their synthesis complicated or even impossible. For example, Fe$_3$IrN becomes stable above 37 GPa, meaning that high pressure is probably needed for its synthesis. Nevertheless, its high cohesion energy [42]

signifies that if successfully synthesized, Fe$_3$IrN is supposed to remain stable for a long time. Nevertheless, all the stability calculations were done for bulk crystals [33,35], while for application exploiting the ANE, thin films would preferably be used. Therefore, we presume that when using an appropriate substrate, some of the Fe$_3$(Ru,Rh,Os,Ir)N compounds can be prepared in the form of a thin layer.

All theoretical works show that all Fe$_3$(Ru,Rh,Os,Ir)N compounds are metallic and ferromagnetic (FM) [31–42]. Importantly, the Curie temperature stays above room temperature, as confirmed by experiments [28,29] (see Table I). These features are thus promising for a high ANE at room temperature in these compounds.

Here, we theoretically study the ANE in the Fe$_3M$N series (M = Ru, Rh, Os, Ir). In order to further increase the ANE, we modify the number of electrons by a rigid shift of the chemical potential, and yet more realistically by further ionic substitutions.

II. COMPUTATIONAL METHOD

Density-functional theory (DFT) calculations using the Vienna *ab initio* simulation package (VASP) [44,45] were carried out with a k mesh of $20 \times 20 \times 20$ points and a plane-wave cutoff of 600 eV. The projector-augmented wave [46] potentials with the generalized gradient approximation [47] were used.

According to the Onsager reciprocal relations [48,49], the longitudinal and transverse transport coefficients, namel, the longitudinal conductivity σ_{xx}, the Hall conductivity σ_{xy}, the Seebeck coefficient S_{xx}, and the Nernst coefficient S_{xy} are linked with the Nernst conductivity α_{xy} by the formula

$$\alpha_{xy} = \sigma_{xx}S_{xy} + \sigma_{xy}S_{xx}. \tag{2}$$

Here, we are interested in the anomalous Nernst conductivity (ANC) α_{xy}^A, so all off-diagonal quantities in Eq. (2) are considered as anomalous. The quantities on the right-hand side of Eq. (2) are measurable, while α_{xy}^A can be calculated.

To explore the anomalous Hall conductivity (AHC) σ_{xy}^A and the ANC α_{xy}^A, a tight-binding model was constructed from

TABLE I. Stoichiometry, magnetic order (FM = ferromagnetic, FI = ferrimagnetic), Curie temperature, experimental (at room temperature) and optimized lattice parameter of the studied phases, and magnetic moment for Fe at the $3c$ site, for substituted $3d$ metal at the $3c$ site, for Fe or $4d$ or $5d$ metal at the $1a$ site (see Fig. 1), and total magnetic moment.

Stoichiometry and magnetic order		T_C (°C)	Lattice parameter a (Å)		Magnetic moment (μ_B)			
			Experimental	Optimized	$3c$ (Fe)	$3c$ (M)	$1a$	Total
α-Fe	(FM)	769	2.87	2.87	2.25	2.25	2.25	9.00
γ-Fe	(FM)			3.49	1.03	1.03	1.03	4.12
Fe$_4$N	(FM)	488 [43]	3.80	3.79	2.35		2.97	9.94
Fe$_3$RuN	(FM)	470 (Ru$_{0.2}$) [28]		3.80	2.20		0.80	7.39
Fe$_3$RhN	(FM)	≈232 [29]	3.83	3.84	2.61		0.96	8.75
Fe$_3$OsN	(FM)	466 (Os$_{0.2}$) [28]		3.79	2.00		0.50	6.53
Fe$_3$IrN	(FM)	462 (Ir$_{0.2}$) [28]		3.82	2.36		0.59	7.69
Fe$_3$MoN	(FI)			3.78	1.26		−0.20	3.59
Fe$_2$CrRuN	(FI)			3.81	2.06	−1.67	0.67	3.13
Fe$_2$MnRuN	(FI)			3.82	2.26	−2.41	0.58	2.69
Fe$_2$MnRuN	(FM)			3.82	2.09	2.16	0.52	6.83

the DFT bands using the WANNIER90 package [50], including the TM-p, d, and N-p characters as a basis set. The Brillouin zone (BZ) was sampled by $500 \times 500 \times 500$ division for the calculations of the Berry curvature $\mathbf{\Omega}(\mathbf{k})$. We set the magnetization along [001] for the cubic materials, hence only the z component $\Omega^z(\mathbf{k}) = \sum_n f_{n\mathbf{k}} \Omega_n^z(\mathbf{k})$ is nonzero ($f_{n\mathbf{k}}$ is the Fermi-Dirac distribution function, and n is the band index), which can be expressed by Kubo formalism [51],

$$\Omega_n^z(\mathbf{k}) = -\sum_{n' \neq n} \frac{2\hbar \, \mathrm{Im} \langle \psi_{n\mathbf{k}} | v_x | \psi_{n'\mathbf{k}} \rangle \langle \psi_{n'\mathbf{k}} | v_y | \psi_{n\mathbf{k}} \rangle}{(\varepsilon_{n'\mathbf{k}} - \varepsilon_{n\mathbf{k}})^2}, \quad (3)$$

where $\varepsilon_{n\mathbf{k}}$ is the electron energy, v's are velocity operators, and ψ's are the Bloch wave functions. The intrinsic AHC is obtained by integration of $\Omega^z(\mathbf{k})$ over the BZ,

$$\sigma_{xy}^A = -\frac{e^2}{\hbar} \int_{BZ} \frac{d\mathbf{k}}{(2\pi)^3} \Omega^z(\mathbf{k}). \quad (4)$$

Zero-temperature limit of the AHC was used, which was basically indistinguishable from using the finite-temperature AHC in our calculations. This allows one to formally introduce an auxiliary quantity—an energy-dependent AHC

$$\sigma_{xy}^A(\varepsilon) = -\frac{e^2}{\hbar} \int_{BZ} \frac{d\mathbf{k}}{(2\pi)^3} \sum_{\varepsilon_{n\mathbf{k}} < \varepsilon} \Omega_n^z(\mathbf{k}), \quad (5)$$

describing contributions to the AHC by electrons with energies lower than some given energy ε. The intrinsic ANC at T is obtained by the following expression [52]:

$$\alpha_{xy}^A(T) = -\frac{1}{e} \int d\varepsilon \frac{\partial f}{\partial \mu} \sigma_{xy}^A(\varepsilon) \frac{\varepsilon - \mu}{T}, \quad (6)$$

where $f(\frac{\varepsilon - \mu}{T})$ is the Fermi-Dirac distribution function, μ being the chemical potential. Interestingly, the ANC at low temperatures can be approximated using the Sommerfeld expansion as

$$\alpha_{xy}^A(T) \approx \frac{\pi^2}{3} \frac{k_B^2 T}{e} \frac{d\sigma_{xy}^A(\varepsilon)}{d\varepsilon} \bigg|_{\varepsilon = \varepsilon_F}. \quad (7)$$

This helps with interpretation of the results: At low temperatures, the ANC is proportional to the derivative of $\sigma_{xy}^A(\varepsilon)$ at the Fermi energy ε_F. At finite temperatures, electrons in the energy window $\approx 3k_B T$ contribute to the ANC [53]. Therefore, the magnitude of the ANC at T is roughly proportional to the difference between the AHC below and above ε_F over the energy range of $\approx \pm 3k_B T$.

We did not consider the orbital moments for each site, because the calculated values are much smaller than $0.1\mu_B$ per site for all the cases in this study.

Let us note, that the temperature scale in our calculation is probably overestimated compared to the realistic value. It was observed in previous works by the comparison of the experimental and the calculated ANC for Co_2MnGa [54] or $CuCr_2X_4$ ($X = S$, Se, Te) [53], that the experimental temperature appears to be about ten times smaller than the numerical one. The authors argued that it is due to the absence of the bandwidth renormalization by strong correlation effects of the d electrons in conventional DFT approaches. The strength of the correlation effects depends on the transition metal elements and their environment. In our case, we assume a similar
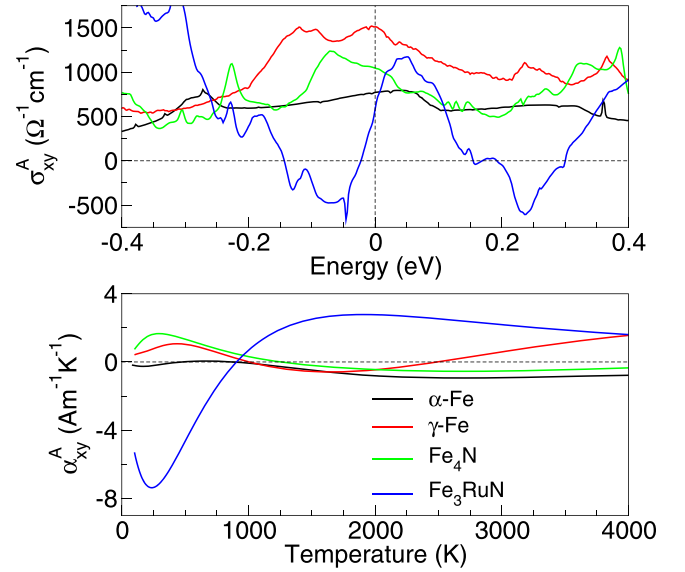

FIG. 2. The calculated energy-dependent AHC (σ_{xy}^A) using Eq. (5) and the temperature-dependent ANC (α_{xy}^A) using Eq. (6) for α-Fe (FM), γ-Fe (FM), Fe_4N (FM), and Fe_3RuN (FM). The Fermi energy is set to zero.

degree of temperature scale renormalization and therefore we have performed the calculation of the ANC over a temperature range up to 4000 K in order to cover the presumed experimental temperature range of several hundreds of degrees.

III. RESULTS AND DISCUSSION

A. ANC and band structures in α-Fe, γ-Fe, Fe_4N, and Fe_3RuN

As the first of the heavy transition metals we tried the isoelectronic substitution of Ru for Fe. Figure 2 shows the comparison of the calculated energy-dependent AHC and the temperature-dependent ANC for martensite α-Fe (bcc), austenite γ-Fe (fcc), Fe_4N, and Fe_3RuN. The structural form stable at room temperature is α-Fe. However, we have also included the high-temperature form γ-Fe (stable above 910 °C), since the structure of Fe_4N is derived from this structure.

The comparison of the calculated ANC for α-Fe, γ-Fe, and Fe_4N shows a substantial increase in the low-temperature range for γ-Fe compared to α-Fe, whereas the increase of the ANC from γ-Fe to Fe_4N is smaller. It suggests that the main enhancement of the ANC is connected with the structural change from a bcc to a fcc-type structure. The insertion of N in Fe_4N further slightly increases ANC, but the main benefit of nitrogen is actually the stabilization of the fcc-type structure at room temperature. It is worth noting that γ-Fe has a much larger ANC than α-Fe despite its magnetic moment being more than two times smaller.

The magnitude of the ANC for specific temperature is related to the difference between the AHC below and above the Fermi energy over the corresponding energy range ($\approx \pm 3k_B T$). It can be seen that the dependence of the AHC on energy for α-Fe is quite flat and therefore its ANC is close to zero over the whole temperature range. The AHC for γ-Fe is enhanced around the Fermi energy and slowly decreases both at low and high energy and becomes flat further from
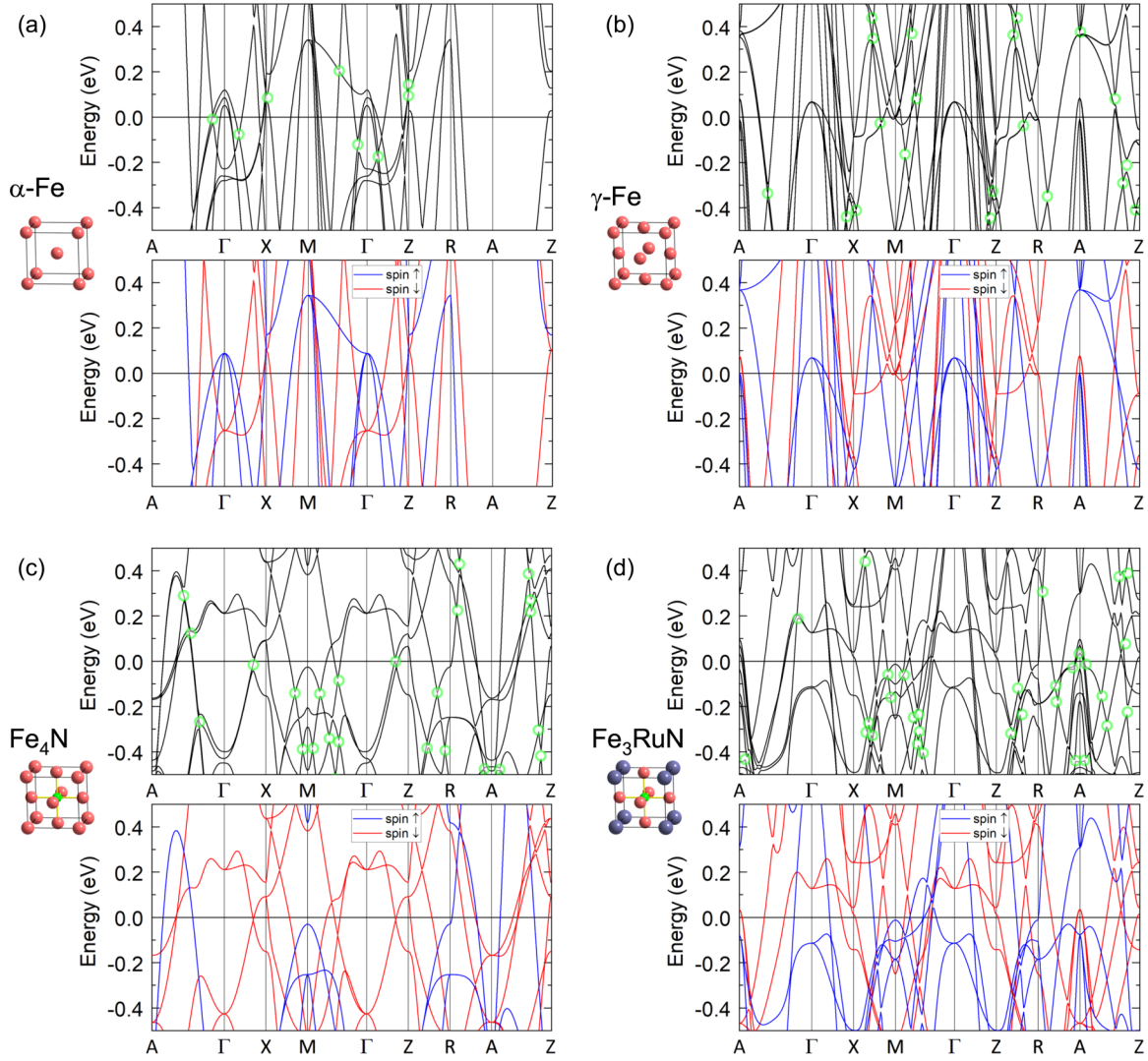
FIG. 3. Band structures of (a) α-Fe (bcc), (b) γ-Fe (fcc), (c) Fe$_4$N, and (d) Fe$_3$RuN. Top: with SOC. Bottom: without SOC, where spin-up bands are plotted as blue lines and spin-down bands as red lines. The Weyl points are highlighted by green circles. The Fermi energy is set to zero.

ε_F similarly to the AHC of α-Fe. The AHC for Fe$_4$N is also enhanced around the Fermi energy, but its decrease below and above ε_F is steeper compared to that of γ-Fe, whereas the AHC further from ε_F is again quite similar to that of α-Fe. Therefore, magnitudes of the ANC for γ-Fe and Fe$_4$N are elevated at low temperatures, and become comparable with α-Fe for higher temperatures. The dependence for Fe$_3$RuN [see structure in Fig. 1(c)] is significantly different. The AHC displays a big change from -500 to $+1000$ Ω^{-1} cm^{-1} around the Fermi energy. It results in high value of the ANC with maximum (in absolute values) $\alpha_{xy}^A = -8$ A K^{-1} m^{-1} at low temperature. However, for wider energy range the slope of the AHC is reversed, so that the ANC for higher temperature, corresponding to the integration over wider energy range, acquires lower values and even changes the sign.

The origin of high ANC values can be deduced from the band structure around the Fermi energy (see Fig. 3), where a comparison of the band structure along the high-symmetry points is shown for α-Fe, γ-Fe, Fe$_4$N, and Fe$_3$RuN, with and without the SOC. The Weyl points, which are the sources

of the Berry curvature, are highlighted in the figures of the band structure with the SOC. When the structure is changed from α-Fe [Fig. 3(a)] to γ-Fe [Fig. 3(b)] the band structure around the Fermi energy is getting more complex and the number of Weyl points increases. A further small increase of the number of Weyl points compared to γ-Fe is detected for Fe$_4$N [Fig. 3(c)]. However, the fundamental difference occurs between Fe$_4$N and Fe$_3$RuN [Fig. 3(d)], where the increase of Weyl points is much higher below ε_F than above ε_F. This increase of asymmetry creates a large difference in the AHC below and above the Fermi energy, and consequently a large enhancement of the ANC in Fe$_3$RuN as seen in Fig. 2.

B. ANC in Fe$_3$(Rh,Os,Ir)N compared to Fe$_3$RuN

The effect of the substitution by elements neighboring to Ru, namely, Rh, Os, and Ir, for which a strong spin-orbit coupling is also expected, was investigated, too (see Fig. 4). Maximum value up to $\alpha_{xy}^A \approx 4$ A K^{-1} m^{-1} was obtained for isoelectronic substitution of Os. Substitution of Rh or Ir for
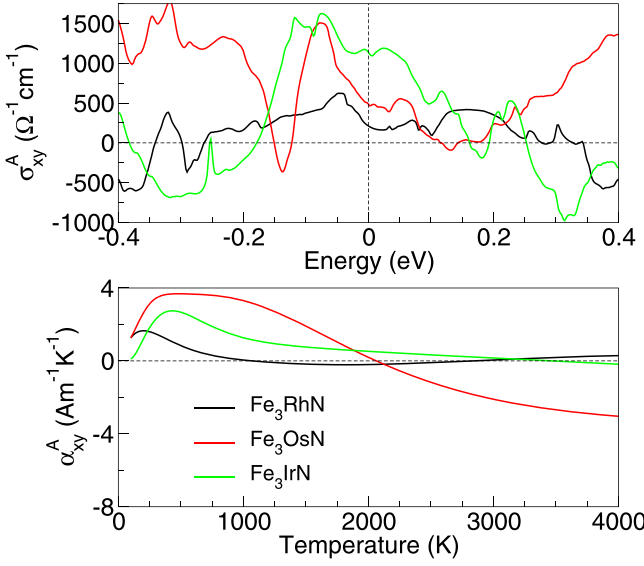
FIG. 4. The calculated energy-dependent AHC (σ_{xy}^A) using Eq. (5) and the temperature-dependent ANC (α_{xy}^A) using Eq. (6) for Fe$_3$RhN (FM), Fe$_3$OsN (FM), and Fe$_3$IrN (FM). The Fermi energy is set to zero.

Fe, which adds one extra electron to the structure, resulted in even lower ANC values. All these substitutions lead to positive ANC values at low temperatures, so in this respect the negative ANC in the case of the Ru substitution is an exception. However, the highest ANC in absolute value was calculated in the case of Ru substitution, so we further focused on this case for a more detailed investigation.

Our calculated $\alpha_{xy}^A = -8$ A K^{-1} m^{-1} for Fe$_3$RuN is comparable in absolute value with the record experimental ANCs so far obtained, e.g., 10 A K^{-1} m^{-1} for Co$_3$Sn$_2$S$_2$ [55], 15 A K^{-1} m^{-1} for UCo$_{0.8}$Ru$_{0.2}$Al [26], or 10 A K^{-1} m^{-1} for a canted antiferromagnet YbMnBi$_2$ [27]. However, all these compounds have critical temperatures of magnetic ordering below room temperature. In distinction, iron nitrides display critical temperatures several hundreds of degrees above room temperature, namely, $T_C = 488$ °C for Fe$_4$N (see Table I). The critical temperature diminishes by doping, nevertheless it remains sufficiently above room temperature, e.g., $T_C = 232$ °C for Fe$_3$RhN [29]. In the case of Fe$_3$RuN, the experimental T_C was only determined for low doping $x = 0.2$ to be 470 °C [28], and we can anticipate that the dependence of T_C on doping will show a similar decrease as for Fe$_3$RhN.

C. Rigid shift of μ in Fe$_3$RuN

To find good performance in the ANC, it is important to get a big change in the AHC around the Fermi energy. This can be achieved by electron/hole doping to find the best position of the chemical potential. Figure 5 shows the results of the rigid shift of μ in Fe$_3$RuN. Both electron and hole doping show dramatic changes of the ANC from negative to positive values at low-temperature regime. For the hole doping, α_{xy}^A is maximized at one hole/f.u. at -0.12 eV, while the electron doping shows rather a smaller maximum at 0.5 electrons/f.u. ($+0.12$ eV). Moreover, the hole doping shows quite high
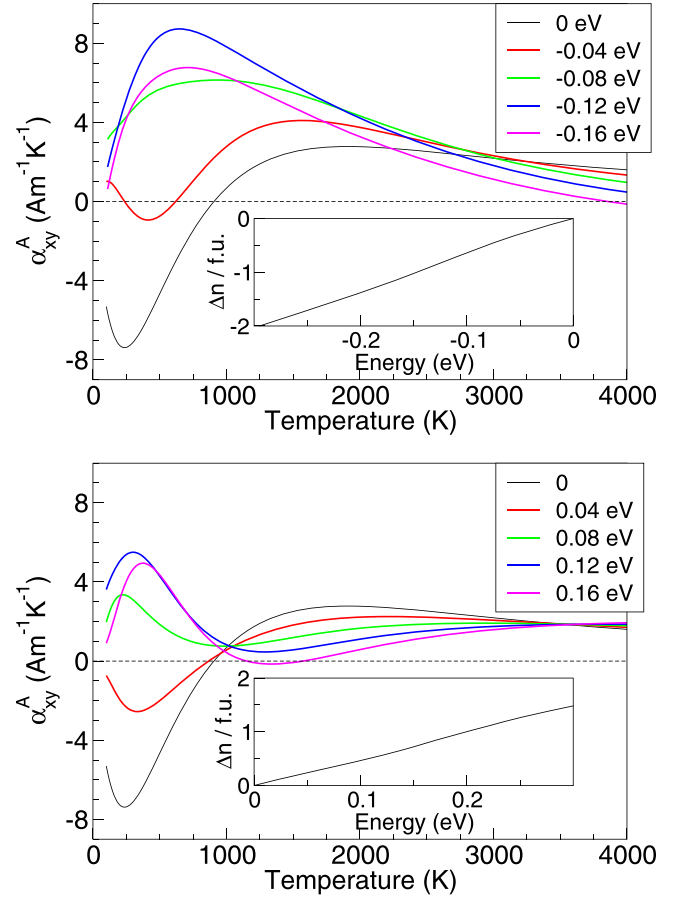

FIG. 5. The calculated temperature-dependent ANC (α_{xy}^A) using Eq. (6) with a rigid shift of μ for Fe$_3$RuN. Insets: The amount of doping level Δn/f.u. as a function of μ. Here, Δn/f.u. is given by the number of (top) holes and (bottom) electrons per formula units.

values of the ANC over a broader temperature range compared to electron doping.

D. ANC in Fe$_3$RuN substituted by Mo, Cr, and Mn

The maximum ANC is achieved for rather high doping level, for which the rigid shift approximation is hardly valid. To simulate a more realistic shift of the chemical potential, we have calculated several substituted structures. We have focused on the hole doping, which appeared more promising using the approach of a rigid shift of μ. Therefore we have tested Cr, Mn, and Mo as substituting elements into Fe$_3$RuN, since these elements have less valence d electrons than Fe or Ru. The doping level of one hole/f.u. corresponds to Fe$_2$MnRuN, and two holes/f.u. arises in Fe$_3$MoN and Fe$_2$CrRuN. Here, Cr and Mn replace Fe at site (1/2,1/2,0), while Mo replaces Ru at site (0,0,0), based on relative ionic sizes.

All the substituted compounds were found to have ferrimagnetic (FI) ground state, with the substituted ion (Mo,Cr,Mn) having opposite spin polarization relative to the majority spin. In the case of Fe$_2$MnRuN, the FM solution was also found to be locally stable, but with 443 meV/f.u. higher energy than the FI one.
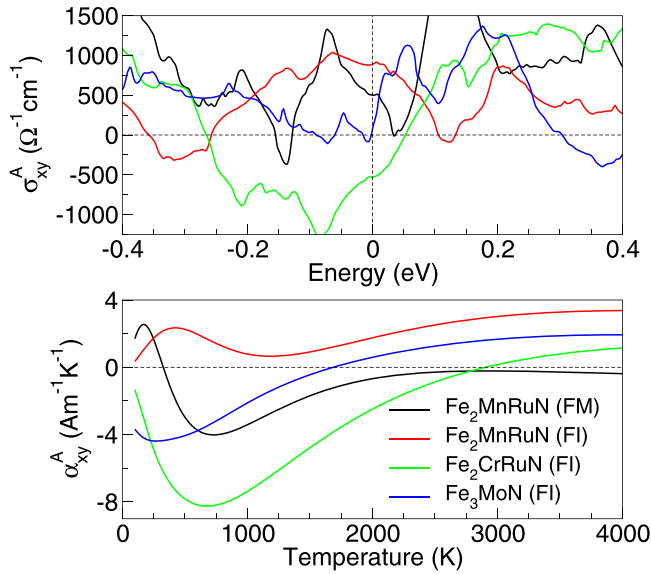
FIG. 6. The calculated energy-dependent AHC (σ_{xy}^A) using Eq. (5) and the temperature-dependent ANC (α_{xy}^A) using Eq. (6) for Fe$_2$MnRuN (one hole/f.u., FM and FI), Fe$_2$CrRuN (two holes/f.u., FI), and Fe$_3$MoN (two holes/f.u., FI). The Fermi energy is set to zero.
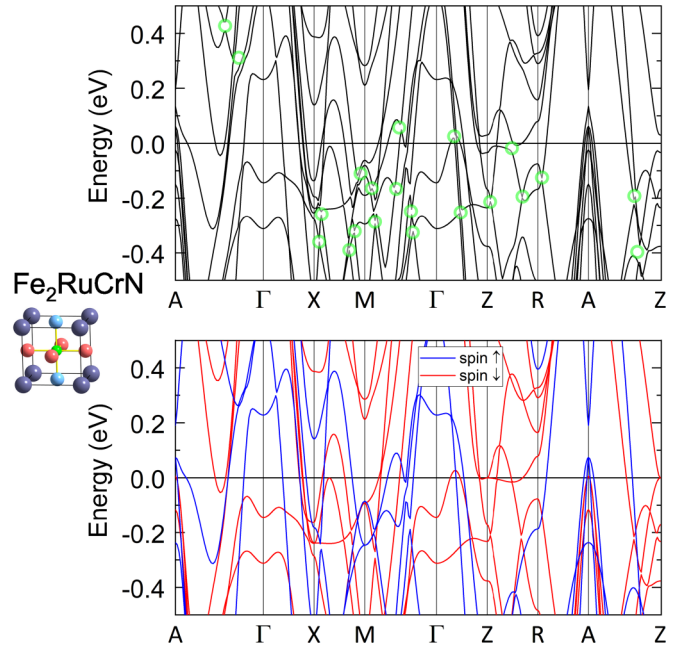

FIG. 7. Band structure of Fe$_2$RuCrN. Top: with SOC. Bottom: without the SOC, where spin-up bands are plotted as blue lines and spin-down bands as red lines. The Weyl points are highlighted by green circles. The Fermi energy is set to zero.

The ground state change shows limitations of the rigid shift approximation, thus the calculated ANC using the rigid shift model with $\Delta\mu = -0.12$ eV (one hole/f.u.) in Fig. 5 can be compared only to the metastable FM solution of Fe$_2$MnRuN (one hole/f.u. from Fe$_3$RuN) in Fig. 6. Even if the two approaches consider the FM state, they give completely different results. While the rigid shift model calculation results in positive ANC over the whole temperature range with maximum up to 8 A K^{-1} m^{-1}, the calculation for the doubly substituted structure gives mostly negative ANC with maximum -4 A K^{-1} m^{-1}. Clearly, the rigid shift model cannot be applied for such high doping level, since the band structure itself is also going to be significantly altered. Interestingly, the stable FI solution of Fe$_2$MnRuN gives positive ANC over the whole temperature range similarly to the rigid shift model keeping FM order, but the maximum ANC is much smaller. Both substitutions simulating two holes/f.u. doping give negative ANC at low temperature with changing sign at high temperature.

Among the above substitutions, Fe$_2$RuCrN [see the structure in Fig. 1(d)] appears to be the most promising, as it shows the ANC with maximum -8 A K^{-1} m^{-1} similar to Fe$_3$RuN, but with persisting high values over a broader temperature range. The band structure of Fe$_2$RuCrN is shown in Fig. 7. It seems that the important difference from the Fe$_3$RuN band structure does not consist in the total number of Weyl points. Rather, it is the difference in their number above and below the Fermi level that is significant, more specifically the smaller number of Weyl points above ε_F. Therefore, we propose Fe$_2$RuCrN as a starting stoichiometry for further experimental study of candidates for devices possessing a high ANE and suitable for room- and high-temperature applications. It is worth noting that since the magnetic arrangement of Fe$_2$RuCrN is FI, the total magnetic moment is about three times lower than that of FM Fe$_4$N, nevertheless, the maximum absolute value of the ANC is about four times higher for Fe$_2$RuCrN compared to Fe$_4$N.

IV. CONCLUSIONS

In our work, we have calculated the ANC for Fe$_4$N substituted with several 4d and 5d transition metals with a strong spin-orbit coupling. The strongest ANC of -8 A K^{-1} m^{-1} was calculated for Ru-substituted iron nitride Fe$_3$RuN with maximum value appearing at low temperature. Comparable ANCs have already been observed, but only for compounds with critical temperatures below room temperature [26,27,55]. In order to further improve the ANC performance, we have tested electron and hole doping by rigid shift of the chemical potential. Hole doping appeared to be more auspicious, therefore we have tried to simulate a more realistic shift of the chemical potential by substitution of elements with lower number of d electrons. A similar maximum high value as for Fe$_3$RuN, but persisting to higher temperatures, was found for Fe$_2$RuCrN.

Altogether, our work shows that iron nitrides with antiperovskite structure optimized by proper substitutions are promising systems for transverse thermoelectric applications. An important advantage of iron nitrides is the critical temperature high above room temperature. The most promising system is Fe$_2$RuCrN, which we propose as a starting stoichiometry for further experimental study of candidates for devices with a high anomalous Nernst effect and suitable for room- and high-temperature applications. We stress another advantage of this material, that it is composed from nontoxic, and except for Ru, also fairly abundant elements.

[1] J. M. Gallego, S. Y. Grachev, D. M. Borsa, D. O. Boerma, D. Écija, and R. Miranda, Mechanisms of epitaxial growth and magnetic properties of γ'-Fe$_4$N(100) films on Cu(100), Phys. Rev. B **70**, 115417 (2004).

[2] T. K. Kim and M. Takahashi, New magnetic material having ultrahigh magnetic moment, Appl. Phys. Lett. **20**, 492 (1972).

[3] Y. Sugita, K. Mitsuoka, M. Komuro, H. Hoshiya, Y. Kozono, and M. Hanazono, Giant magnetic moment and other magnetic properties of epitaxially grown Fe$_{16}$N$_2$ single-crystal films (invited), J. Appl. Phys. **70**, 5977 (1991).

[4] T. Takahashi, J. Burghaus, D. Music, R. Dronskowski, and J. M. Schneider, Elastic properties of γ'-Fe$_4$N probed by nanoindentation and *ab initio* calculation, Acta Mater. **60**, 2054 (2012).

[5] C.-H. Cheng, M.-T. Nguyen, T.-S. Leu, I.-L. Chang, M.-L. Liao, S. V. Panin, and A. V. Panin, Magnetic and mechanical properties of deformed iron nitride γ'-Fe$_4$N, J. Appl. Math. **2015**, 238730 (2015).

[6] B. Yu, L. Lin, B. Ma, Z. Z. Zhang, Q. Y. Jin, and J. P. Wang, Fabrication and physical properties of [Fe/Fe$_4$N]$_N$ multilayers with high saturation magnetization, AIP Adv. **6**, 056108 (2016).

[7] A. Samanta, H. Chakraborty, M. Bhattacharya, J. Ghosh, M. Sreemany, S. Bysakh, R. Rane, A. Joseph, G. Jhala, S. Mukherjee, M. Das, and A. K. Mukhopadhyay, Nanotribological response of a plasma nitrided bio-steel, J. Mech. Behav. Biomed. Mater. **65**, 584 (2017).

[8] A. W. Machlet, Hardening or treatment of steel, iron, US Patent No. US1092925A (April 14, 1914).

[9] A. Fry, Process for hardening steel alloys, US Patent No. US1487554A (March 18, 1924).

[10] S. Bhattacharyya, Iron nitride family at reduced dimensions: A review of their synthesis protocols and structural and magnetic properties, J. Phys. Chem. C **119**, 1601 (2015).

[11] I. Dirba, P. Komissinskiy, O. Gutfleisch, and L. Alff, Increased magnetic moment induced by lattice expansion from α-Fe to α'-Fe$_8$N, J. Appl. Phys. **117**, 173911 (2015).

[12] I. Dirba, M. Baghaie Yazdi, A. Radetinac, P. Komissinskiy, S. Flege, O. Gutfleisch, and L. Alff, Growth, structure, and magnetic properties of γ'-Fe$_4$N thin films, J. Magn. Magn. Mater. **379**, 151 (2015).

[13] Y. Chen, D. Gölden, I. Dirba, M. Huang, O. Gutfleisch, P. Nagel, S. Schuppler M. Merz, G. Schütz, L. Alff, and E. Goering, Element-resolved study on the evolution of magnetic response in Fe$_x$N compounds, J. Magn. Magn. Mater. **498**, 166219 (2020).

[14] I. Dirba, C. K. Chandra, Y. Ablets, J. Kohout, T. Kmječ, O. Kaman, and O. Gutfleisch, Evaluation of Fe-nitrides, -borides and -carbides for enhanced magnetic fluid hyperthermia with experimental study of α''-Fe$_{16}$N$_2$ and ϵ-Fe$_3$N nanoparticles, J. Phys. D: Appl. Phys. **56**, 025001 (2023).

[15] S. Isogami, K. Takanashi, and M. Mizuguchi, Dependence of anomalous Nernst effect on crystal orientation in highly ordered γ'-Fe$_4$N films with anti-perovskite structure, Appl. Phys. Express **10**, 073005 (2017).

[16] K. Ito, J. Wang, Y. Shimada, H. Sharma, M. Mizuguchi, and K. Takanashi, Enhancement of the anomalous Nernst effect in epitaxial Fe$_4$N films grown on SrTiO$_3$(001) substrates with oxygen deficient layers, J. Appl. Phys. **132**, 133904 (2022).

[17] Y. Sakuraba, Potential of thermoelectric power generation using anomalous Nernst effect in magnetic materials, Scr. Mater. **111**, 29 (2016).

[18] M. Mizuguchi and S. Nakatsuji, Energy-harvesting materials based on the anomalous Nernst effect, Sci. Technol. Adv. Mater. **20**, 262 (2019).

[19] A. Sakai, S. Minami, T. Koretsune, T. Chen, T. Higo, Y. Wang, T. Nomoto, M. Hirayama, S. Miwa, D. Nishio-Hamane, F. Ishii, R. Arita, and S. Nakatsuji, Iron-based binary ferromagnets for transverse thermoelectric conversion, Nature (London) **581**, 53 (2020).

[20] J. Wang, A. Miura, R. Modak, Y. K. Takahashi, and K. Uchida, Magneto-optical design of anomalous Nernst thermopile, Sci. Rep. **11**, 11228 (2021).

[21] G. Lopez-Polin, H. Aramberri, J. Marques-Marchan, B. I. Weintrub, K. I. Bolotin, J. I. Cerdá, and A. Asenjo, High-power-density energy-harvesting devices based on the anomalous Nernst effect of Co/Pt magnetic multilayers, ACS Appl. Energy Mater. **5**, 11835 (2022).

[22] H. K. Singh, I. Samathrakis, C. Shen, and H. Zhang, Giant anomalous Hall and anomalous Nernst conductivities in antiperovskites and their tunability via magnetic fields, Phys. Rev. Mater. **6**, 045402 (2022).

[23] H. Jacobs, D. Rechenbach, and U. Zachwieja, Structure determination of γ'-Fe$_4$N and ϵ-Fe$_3$N, J. Alloys Compd. **227**, 10 (1995).

[24] S. K. Chen, S. Jin, T. H. Tiefel, Y. F. Hsieh, E. M. Gyorgy, and D. W. Johnson, Jr., Magnetic properties and microstructure of Fe$_4$N and (Fe,Ni)$_4$N, J. Appl. Phys. **70**, 6247 (1991).

[25] C. Fu, Y. Sun, and C. Felser, Topological thermoelectrics, APL Mater. **8**, 040913 (2020).

[26] T. Asaba, V. Ivanov, S. M. Thomas, S. Y. Savrasov, J. D. Thompson, E. D. Bauer, and F. Ronning, Colossal anomalous Nernst effect in a correlated noncentrosymmetric kagome ferromagnet, Sci. Adv. **7**, eabf1467 (2021).

[27] Y. Pan, C. Le, B. He, S. J. Watzman, M. Yao, J. Gooth, J. P. Heremans, Y. Sun, and C. Felser, Giant anomalous Nernst signal in the antiferromagnet YbMnBi$_2$, Nat. Mater. **21**, 203 (2022).

[28] D. Andriamandroso, S. Matar, G. Demazeau, and L. Fournes, Morphological and magnetic properties of Ru, Os and Ir-substituted Fe$_4$N, IEEE Trans. Magn. **29**, 2 (1993).

[29] A. Houben, P. Müller, J. von Appen, H. Lueken, R. Niewa, and R. Dronskowski, Synthesis, crystal structure, and magnetic properties of the semihard itinerant ferromagnet RhFe$_3$N, Angew. Chem. Int. Ed. **44**, 7212 (2005).

[30] A. Houben, V. Šepelák, K.-D. Becker, and R. Dronskowski, Itinerant ferromagnet RhFe$_3$N: Advanced synthesis and ^{57}Fe Mössbauer analysis, Chem. Mater. **21**, 784 (2009).

[31] Z. Wu and J. Meng, Elastic and electronic properties of CoFe$_3$N, RhFe$_3$N, and IrFe$_3$N from first principles, Appl. Phys. Lett. **90**, 241901 (2007).

[32] J. C. Krause and C. Paduani, Ferromagnetism of OsFe$_3$N, Phys. B (Amsterdam, Neth.) **367**, 282 (2005).

[33] J. von Appen and R. Dronskowski, Predicting new ferromagnetic nitrides from electronic structure theory: IrFe$_3$N and RhFe$_3$N, Angew. Chem. Int. Ed. **44**, 1205 (2005).

[34] S. F. Matar, A. Houari, M. A. Belkhir, and M. Zakhour, Covalent magnetism and invar-like behavior within ternary nitrides: An *ab initio* study, Z. Naturforsch. B: J. Chem. Sci. **62**, 881 (2007).

[35] E. Zhao, H. Xiang, J. Meng, and Z. Wu, First-principles investigation on the elastic, magnetic and electronic properties of MFe$_3$N (M=Fe, Ru, Os), Chem. Phys. Lett. **449**, 96 (2007).

[36] A. V. dos Santos and C. A. Kuhnen, Electronic structure and magnetic properties of RuFe$_3$N nitride, J. Solid State Chem. **182**, 3183 (2009).

[37] C. Paduani, First-principles calculations of the electronic structure and magnetic properties of the IrFe$_3$N nitride, Phys. Status Solidi B **241**, 2923 (2004).

[38] S. Puvaneswari, G. Sudha Priyanga, R. Rajeswarapalanichamy, and M. Santhosh, *Structural, Electronic, Elastic and Magnetic Properties of* RuFe$_3$N *and* OsFe$_3$N: *A First Principle Study*, AIP Conf. Proc. No. 1665 (AIP, Melville, NY, 2015), p. 030009.

[39] C. Paduani, Electronic structure of the perovskite-type nitride RuFe$_3$N, J. Magn. Magn. Mater. **278**, 231 (2004).

[40] K. Hocine, M. Rabah, D. Rached, S. Djili, and H. Baltache, *Ab initio* study of electronic structure and magnetic properties of MFe$_3$N (M = Ru and Os), Comput. Mater. Sci. **65**, 6 (2012).

[41] Y. Zhang, Z. Wang, and J. Cao, Predicting magnetostriction of MFe$_3$N (M = Fe, Mn, Ir, Os, Pd, Rh) from *ab initio* calculations, Comput. Mater. Sci. **92**, 464 (2014).

[42] A. V. dos Santos, Consequences on the electronic structure and hyperfine of iridium–iron alloys when transformed into substituted iron iridium nitrides, J. Mater. Res. **29**, 959 (2014).

[43] B. C. Frazer, Magnetic Structure of Fe$_4$N, Phys. Rev. **112**, 751 (1958).

[44] G. Kresse and J. Furthmüller, Efficiency of *ab-initio* total energy calculations for metals and semiconductors using a plane-wave basis set, Comput. Mater. Sci. **6**, 15 (1996).

[45] G. Kresse and J. Furthmüller, Efficient iterative schemes for *ab initio* total-energy calculations using a plane-wave basis set, Phys. Rev. B **54**, 11169 (1996).

[46] G. Kresse and D. Joubert, From ultrasoft pseudopotentials to the projector augmented wave method, Phys. Rev. B **59**, 1758 (1999).

[47] J. P. Perdew, K. Burke, and M. Ernzerhof, Generalized Gradient Approximation Made Simple, Phys. Rev. Lett. **77**, 3865 (1996).

[48] L. Onsager, Reciprocal relations in irreversible processes I, Phys. Rev. **37**, 405 (1931).

[49] L. Onsager, Reciprocal relations in irreversible processes II, Phys. Rev. **38**, 2265 (1931).

[50] A. A. Mostofi, J. R. Yates, G. Pizzi, Y.-S. Lee, I. Souza, D. Vanderbilt, and N. Marzari, An updated version of wannier90: A tool for obtaining maximally-localised Wannier functions, Comput. Mater. Sci. **185**, 2309 (2014).

[51] D. J. Thouless, M. Kohmoto, M. P. Nightingale, and M. den Nijs, Quantized Hall Conductance in a Two-Dimensional Periodic Potential, Phys. Rev. Lett. **49**, 405 (1982).

[52] D. Xiao, Y. Yao, Z. Fang, and Q. Niu, Berry-Phase Effect in Anomalous Thermoelectric Transport, Phys. Rev. Lett. **97**, 026603 (2006).

[53] K. H. Ahn, M. Soroka, P. Levinský, V. Kucek, J. Navrátil, K. Knížek, and J. Hejtmánek, Thermal transport in CuCr$_2$X$_4$ (X = S, Se, Te), experiment and *ab initio* calculation, Phys. Rev. B **104**, 085146 (2021).

[54] A. Sakai, Y. P. Mizuta, A. A. Nugroho, R. Sihombing, T. Koretsune, M.-T. Suzuki, N. Takemori, R. Ishii, D. Nishio-Hamane, R. Arita, P. Goswami, and S. Nakatsuji, Giant anomalous Nernst effect and quantum-critical scaling in a ferromagnetic semimetal, Nat. Phys. **14**, 1119 (2018).

[55] H. Yang, W. You, J. Wang, J. Huang, C. Xi, X. Xu, C. Cao, M. Tian, Z.-A. Xu, J. Dai, and Y. Li, Giant anomalous Nernst effect in the magnetic Weyl semimetal Co$_3$Sn$_2$S$_2$, Phys. Rev. Mater. **4**, 024202 (2020).